An Experimental Benchmark of Non-metallic Inclusion Distribution Inside a Heavy Continuous-Casting Slab

ZHONGQIU LIU, BAOKUAN LI, MENGHUAI WU, GUODONG XU, XIAOMING RUAN, and ANDREAS LUDWIG

Different mathematical models were suggested to calculate the transport phenomena of non-metallic inclusions during continuous casting of steel, but there are no experimental data at the process scale available to evaluate the models. This paper is to provide an experimental benchmark to evaluate those models. It includes the most necessary casting process parameters for a heavy continuous-casting (CC) slab and the final result on the spatial and size distribution of macroscopic non-metallic inclusions (MNMIs) in the as-cast slab. The MNMIs with diameter larger than 50 μm inside the CC slab were *in situ* detected through a fast-detection platform (FDP). The casting sample (half width of the slab 1150 mm × 300 mm of entire slab thickness × 75 mm in casting direction) were ground slice by slice with the maximum resolution of 1 mm; the morphology of the MNMIs was metallographically analyzed and the number of the MNMIs of difference size classes was counted; finally, the (3D) spatial distribution of MNMIs of difference size classes in the casting sample was reconstructed. Further information about the distribution of MNMIs was reported as well: (1) typical morphologies of independent nearly spherical MNMIs, "bubble + NMIs," irregular-shaped MNMIs, and cluster MNMIs; (2) the size distribution of MNMIs along the thickness direction in both vertical section and bending section; (3) a probability number density function of MNMI diameter.

https://doi.org/10.1007/s11661-018-5079-0
© The Minerals, Metals & Materials Society and ASM International 2019

I. INTRODUCTION

THE study of non-metallic inclusions (NMIs) is of increasing importance since the properties of steel products depend largely on the amount, size, distribution, composition, and morphology of NMI defects that are mainly formed during continuous-casting (CC) process.[1–4] It is generally believed that the transport of NMIs and entrapment of them by the solidified steel shell mainly depend on the turbulent flow, solute concentration, temperature, and solidification of steel in the CC mold.[5–8] Progress in computational fluid dynamics (CFD) techniques allows for the simulation and modeling of NMI transport in complex flow configurations of mold.

Extensive numerical studies of the transport of NMIs inside the CC mold have been performed.[5–13] Pfeiler *et al.*[6] established a general model to describe the motion of particles during solidification in a steel continuous caster, considering the mushy zone morphology (columnar) and various forces acting on particles. Thomas *et al.*[7] considered normal and tangential force balances involving ten different forces acting on an NMI in the solidified front, and the primary dendrite arm spacing (PDAS) was considered for the NMI entrapment. Lee *et al.*[9] studied the effect of thermal Marangoni force for the behavior of argon bubbles at the solidifying interface, revealing that the thermal Marangoni force could play an important role in the entrapment of argon bubbles. Liu *et al.*[10–12] developed a new criterion for particle entrapment in the solidification front. The transient motions of single and cluster NMIs in a vertical-bending caster were studied. Recently, Barati *et al.*[13] established a numerical model to study the transient clogging process of nozzle, indicating that the clogging is a stochastic and

ZHONGQIU LIU is with the School of Metallurgy, Northeastern University, Shenyang, 110819, P.R. China and also with the Chair of Simulation and Modeling of Metallurgical Processes, Department of Metallurgy, Montanuniversität Leoben, 8700 Leoben, Austria. Contact e-mail: liuzq@smm.neu.edu.cn BAOKUAN LI is with the School of Metallurgy, Northeastern University. MENGHUAI WU and ANDREAS LUDWIG are with the Chair of Simulation and Modeling of Metallurgical Processes, Department of Metallurgy, Montanuniversität Leoben. GUODONG XU and XIAOMING RUAN are with the Baoshan Iron & Steel Co., Ltd., Shanghai 201900, P.R. China.

Manuscript submitted September 26, 2018.
Article published online January 2, 2019

self-accelerating process. Nevertheless, errors often appear due to limited accuracy of different numerical methodologies and due to inevitable simplifications introduced in the models. Hence, a direct experimental verification of the numerical models on the NMIs distribution in the real steel billet has gained special importance.

Many researchers have extensively investigated the morphology, composition, and classification of NMIs in real steel billet through various direct detection methods, including metallographic microscope observation (MMO),[2,14–16] scanning electron microscopy (SEM),[4,17,18] ASPEX,[19,20] ultrasonic scanning (US).[8,21] Owing to the cost, time requirements, and sampling difficulties of direct detection methods, the steel cleanliness is generally measured in the steel industries using total oxygen content,[22] nitrogen pick-up,[3] nozzle clogging,[18,23,24] and other indirect methods. In addition, several experimental investigations were carried out to study the transport and entrapment behaviors of NMI particles in hot steel melts[25–28] or cold water.[29,30] Nevertheless, the three-dimensional spatial distribution of NMIs in the real billet, which is needed to evaluate the numerical models, has not yet been reported. The aforementioned capture mechanisms[6–13] of NMIs at the solid–liquid interface cannot be validated.

In the present work, an *in situ* detection of macroscopic non-metallic inclusions (MNMIs) with diameter larger than 50 μm inside a heavy CC slab was conducted on a fast-detection platform. The study aimed to provide an experimental benchmark of three-dimensional MNMI distribution inside the heavy slab for the purpose of evaluation of future numerical models. Most important casting process parameters necessary for numerical models were provided in details.

II. PROCESS DETAILS OF CC PROCESS

The chemical composition of the steel is given in Table I. The molten steel from ladle is poured into a tundish and then flows through a SEN into a water-cooled copper mold. A slide gate system is used to control the molten steel flow rate at the upper nozzle, in which an argon-blowing system is used to prevent suction air and SEN clogging. Some small argon bubbles are sometimes trapped by the solidified shell forming pinhole defects,[8] which is also one of the detection objects in the present work. Inside the CC mold, molten steel freezes against the water-cooled copper mold walls and forms a solidified shell, in which those NMIs cannot escape safely from the mold would be captured, forming various NMI defects. Slab samples were obtained from a heavy slab caster with cross section of 300 × 2300 mm^2. The main specifications of the caster are shown in Table II. The geometric constructions and reference cooling conditions of the submerged entry nozzle (SEN) and the mold are shown in Figures 1 and 2. These data are the basic data for numerical simulations. More details of the process can be found in previous publications.[10–12,31,32]

III. SAMPLING METHODOLOGY AND METALLOGRAPHIC ANALYSIS

In order to obtain the three-dimensional spatial and size distribution of MNMIs in the heavy slab, considering the symmetry of the slab, a half width (~ 1150 mm) of the slab was sampled, as shown in Figure 3. Four sub-samples with the size of 300 mm (width direction) × 300 mm (thickness direction) × 75 mm (casting direction) were cut along the width direction of the slab on the left side of SEN. The

Table I. Chemical Composition of the Steel

Elements	C	Si	Mn	Cr	Al	Nb	Ti	Ca
Mass Pct	0.055	0.25	1.7	0.16	0.035	0.04	0.014	0.0019

Table II. Main Specifications of the Slab Caster

Parameter	Steel Caster	Parameter	Steel Caster
Machine Type	vertical bending	liquidus temperature (K)	1796
Mold Length (m)	0.8	solidus temperature (K)	1760
Vertical Length (m)	2.66	pouring temperature (K)	1821
Machine Length (m)	34.17	argon flow rate (L/min)	9.5
Bending Radius (m)	10	molten steel density (kg/m^3)	7100
Tundish Capacity (t)	65	molten steel viscosity (Pa s)	0.0056
Slab Size (mm)	300 × 2300	molten slag density (kg/m^3)	3000
Casting Speed (m/min)	0.6	molten slag viscosity (Pa s)	0.1
SEN Submergence Depth (mm)	175	inclusion density (kg/m^3)	2700
SEN Outport Angle (deg)	15 downward	mold oscillation frequency (Hz)	0.5 to 5
SEN Outport Sizes (mm)	90 × 54	mold oscillation amplitude (mm)	± 1 to ± 6
Thickness of Liquid Slag (mm)	10		

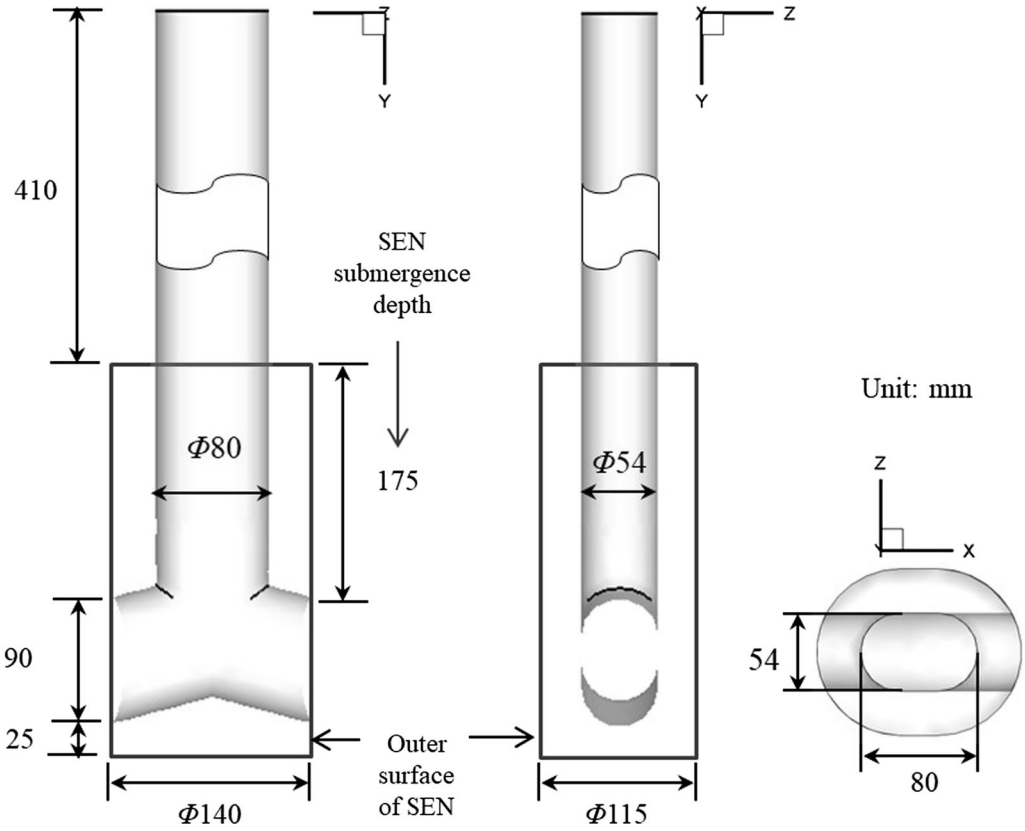

Fig. 1—Geometric constructions of the submerged entry nozzle.

MNMI distribution inside the samples was *in situ* detected directly through a fast-detection platform (FDP), which mainly consists of a vertical-spindle milling machine (Type: X5036), a metallographic microscope, a steel chip collector, *etc*. The steel sample was fixed on the FDP through a base plate, and then it was gradually shaved a thin strip off the edge of the sample along the thickness direction from the outer arc to the inner arc of the slab. In general, the number of MNMIs gradually decreases from the surface region to the inner region of the slab, so a non-uniform shaving scheme was adopted. As shown in Figure 3, for 0 to 15 and 286 to 299 mm from the top wide-face cooling wall (outer arc), the shaving depth is 1 mm. For 16 to 75 and 226 to 285 mm, the shaving depth is 2 mm. For 76 to 225 mm, the shaving depth is 3 mm. The total sampling number for each sub-sample is 139. The sampling area for each layer is 300×75 mm^2. The total sample volume reached 25,875 cubic centimeters, and the total detection area was 125,100 square centimeters. The samples were first observed under an optical microscope with $\times$ 500 scale to mark the locations of all MNMIs larger than 50 μm in diameter. The MNMI morphologies were photographed and transferred to a computer automatically through the data wire. Then these photographs were analyzed by the ImageJ software to get the equivalent diameter of each MNMI.

A total of 2667 MNMIs were found based on the above sampling methodology. Only one large gas bubble with the size of 1930 μm was captured by a curved hook within 0.32 mm beneath the surface of the slab. The formation of such a large bubble was an accidental event, which was not considered in the following statistics of MNMIs. Typical morphologies of MNMIs detected by the optical microscope are shown in Figures 4(a) through (h). A bubble with a shiny surface was observed in Figure 4(a), with a size around 200 μm. This kind of defects is closely related to argon injection during CC process. During the movement of argon bubbles in the liquid pool, the surfaces usually trap a lot of fine solid NMIs, forming typical "bubble + NMIs" defects with the feature that the NMIs are confined in a specific space on the surface of bubble, as shown in Figure 4(b). Dominantly independent nearly spherical MNMIs can be found in a small detection area of samples, as shown in Figure 4(c), the size of MNMIs is between 50 and 150 μm. Sometimes two relatively close MNMIs would collide and aggregate together, forming a bigger MNMI (Figures 4(c) and (e)). In addition, a great deal of irregularly shaped MNMIs was found in the samples, as shown in Figures 4(d) through (f). The MNMI with the morphology shown in Figure 4(e) was treated as a single MNMI, and with the morphology shown in Figure 4(f) was treated as two single MNMIs. A typical cluster NMI is shown in Figure 4(g). This big-cluster NMI was identified as many NMIs with different sizes by the ImageJ software according to the particle boundary. The research object of this work is to identify the MNMIs larger than 50 μm, so two MNMIs were counted. Some chain sulfide MNMIs related to refractory was detected in the samples, as shown in

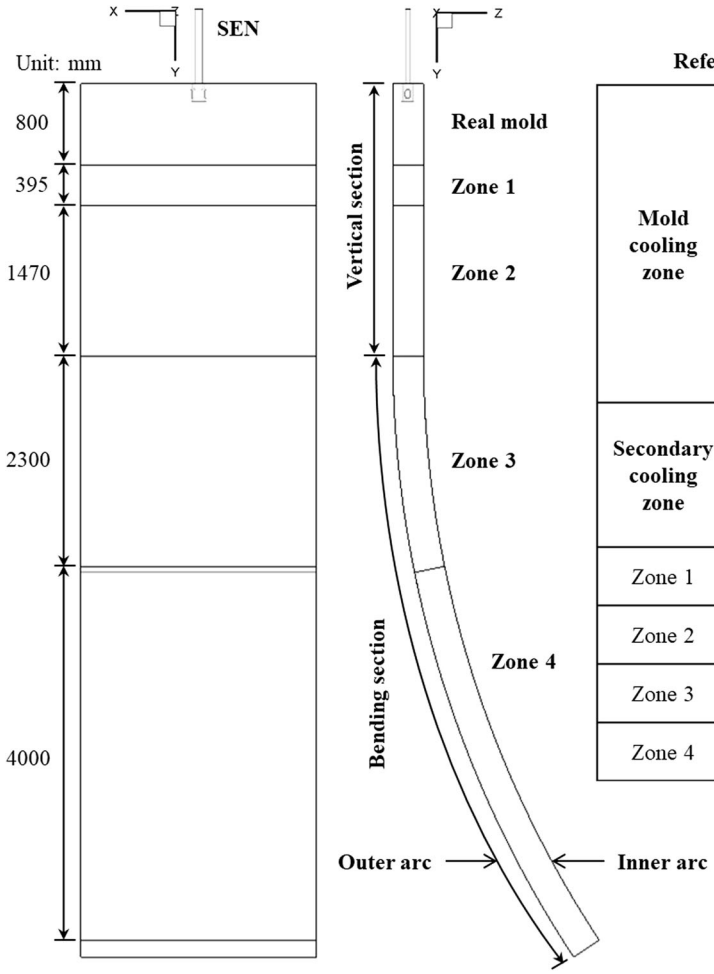

Reference cooling conditions

Mold cooling zone	Heat flux, q [MW·m^{-2}]	
	$q = 2.68 - \psi\sqrt{60h_m / V_C}$	
	where, $\psi = \begin{cases} 0.275 \text{, for wide face} \\ 0.295 \text{, for narrow face} \end{cases}$ h_m is the distance below meniscus, [m] V_c is casting speed, [m/min]	
Secondary cooling zone	Convective heat transfer coefficient, h [W·m^{-2}·K^{-1}]	
	Outer-arc wide face	Inner-arc wide face
Zone 1	699	548
Zone 2	388	308
Zone 3	318	252
Zone 4	309	267

Fig. 2—Geometric constructions and cooling conditions of the mold.

Figure 4(h), with a total length larger than 5 mm. In addition, the shrinkage defects were found in the thickness center of the slab, as shown in Figure 4(i), which were not collected in the present work. Based on the electron microprobe analysis, the typical compositions of MNMIs in the slab samples are alumina-based clusters, silicon oxide spherical NMIs, and irregularly shaped slag NMIs containing calcium oxide, calcium sulfide, and manganese sulfide. It is important to note that the main purpose of the current work is to detect the MNMI distribution inside a slab and to provide an experimental benchmark for evaluation of numerical models. So the details of composition and classification of NMIs are not considered in this work.

IV. MNMI DISTRIBUTION

A. *Spatial Distribution*

In order to obtain the three-dimensional spatial distribution of MNMIs in the slab samples with the same sampling resolution, a simplified data analysis method was adopted based on the assumption of local same distribution of inclusions. D_i refers to the MNMI distribution at layer-i, including locations and sizes. i is the distance from top wide-face cooling wall (outer arc) with value from 1 to 299 mm. Details of data analysis are as follows:

$$D_i = \begin{cases} D_1, D_2 \ldots D_{15} & 1 \le i \le 15 \\ D_{16} = D_{17}, D_{18} = D_{19} \ldots D_{74} = D_{75} & 16 \le i \le 75 \\ D_{76} = D_{77} = D_{78}, D_{79} = D_{80} = D_{81} \ldots D_{223} = D_{224} = D_{225} & 76 \le i \le 225 \\ D_{226} = D_{227}, D_{228} = D_{229} \ldots D_{284} = D_{285} & 226 \le i \le 285 \\ D_{286}, D_{287} \ldots D_{299} & 286 \le i \le 299 \end{cases}, \quad [1]$$

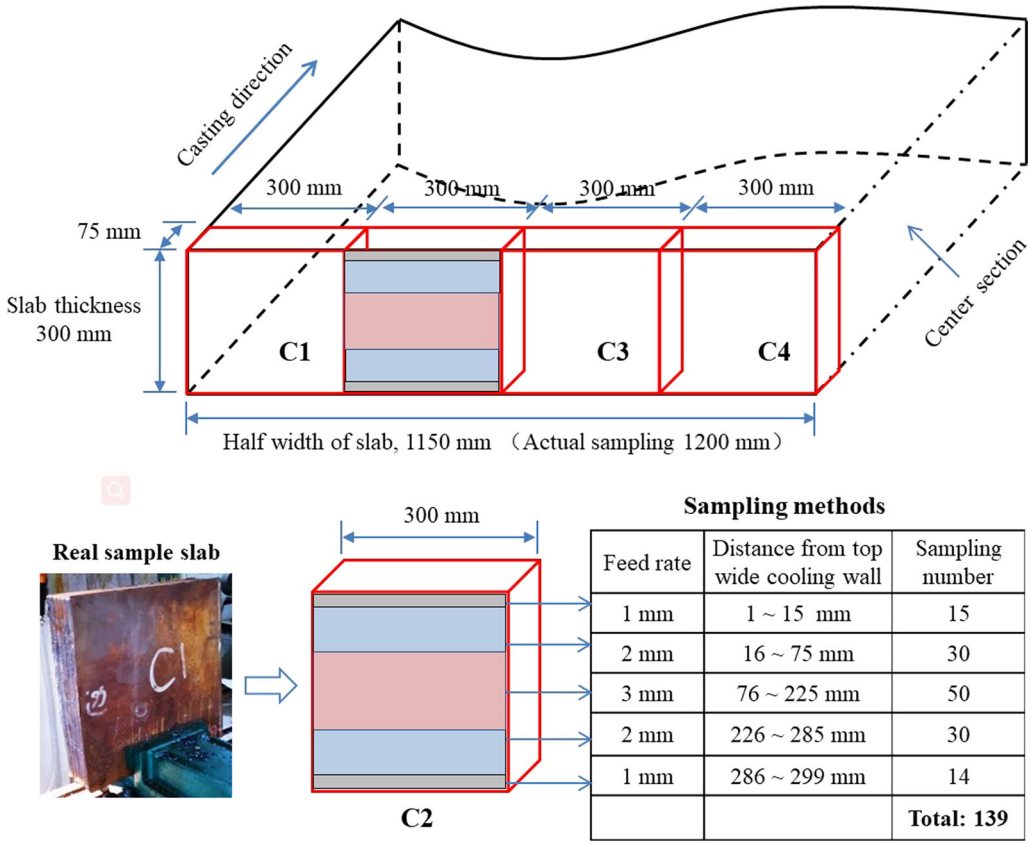

Feed rate	Distance from top wide cooling wall	Sampling number
1 mm	1 ~ 15 mm	15
2 mm	16 ~ 75 mm	30
3 mm	76 ~ 225 mm	50
2 mm	226 ~ 285 mm	30
1 mm	286 ~ 299 mm	14
		Total: 139

Fig. 3—Schematic diagram of sampling in slab.

where the leftmost value of each equal sign is the actual detected MNMI distribution. For example, the D_{78} and D_{77} have the same MNMI distribution with D_{76}.

Considering the hypothetic distributions in some layers, such as D_{17}, D_{78}, D_{227}, a further sampling with 3 millimeters as the sample interval was carried out. Then the MNMI distributions in D_1, D_4, D_7 … D_{292}, D_{295}, D_{298} were used to analyze the spatial distribution of MNMIs in the slab samples with the same sampling resolution, as shown in Figure 5. The *X-coordinate* in the figure refers to the width of the slab, $X = 0$ mm is the location of narrow face, and $X = 1150$ mm is the center. The *Y-coordinate* refers to the casting direction. The *Z-coordinate* refers to the thickness of the slab, $Z = 0$ mm is the outer-arc wall and $Z = 300$ mm is the inner-arc wall. It can be seen that the distribution of MNMIs inside the samples was not uniform and not symmetric. Most MNMIs were captured beneath the wide faces of the slab; fewer MNMIs were captured along the narrow faces and in the thickness center. Several large MNMIs (> 500 μm) were found near the inner-arc wall. One large MNMI (429 μm) was captured at $Z = 181$ mm which is close to the thickness center.

In order to study the MNMI number density distribution in the slab sample, two parameters were defined: the area number density of MNMIs ($N_A[1/cm^2]$) and the volume number density of MNMIs ($N_V[1/cm^3]$). The total detection area in each layer was divided into fifty equal sub-regions along the width direction of the slab with width of 23 mm. The detection area of every sub-region was 75×23 mm^2. Therefore, the area number density of MNMIs can be calculated by:

$$N_{A,j} = \frac{n_j}{7.5 \times 2.3}\,[1/\mathrm{cm}^2], \qquad [2]$$

where n_j is the number of MNMIs in No. j sub-region, j represents the serial number of sub-regions with the value of 1 to 50. The No. 1 sub-region is close to narrow face, and No. 50 is close to width center.

Based on the assumption of uniform distribution of MNMIs inside the sub-region along the thickness direction, the volume number density of MNMIs can be estimated as follows:

$$N_{V,j} = N_{A,j}^{3/2}\,[1/\mathrm{cm}^3]. \qquad [3]$$

The processed results with the same MNMI sampling density shown in Figure 5 are used to analyze the volume number density of MNMIs in the slab samples. Figure 6 shows the volume number density contour of MNMIs in the cross section of the slab, which is mapped based on 50×99 measurement points. Typical banding distributions of MNMIs along the wide direction of the slab were found at different thicknesses of the slab, including 1/6 to 1/4 and the center of thickness. The

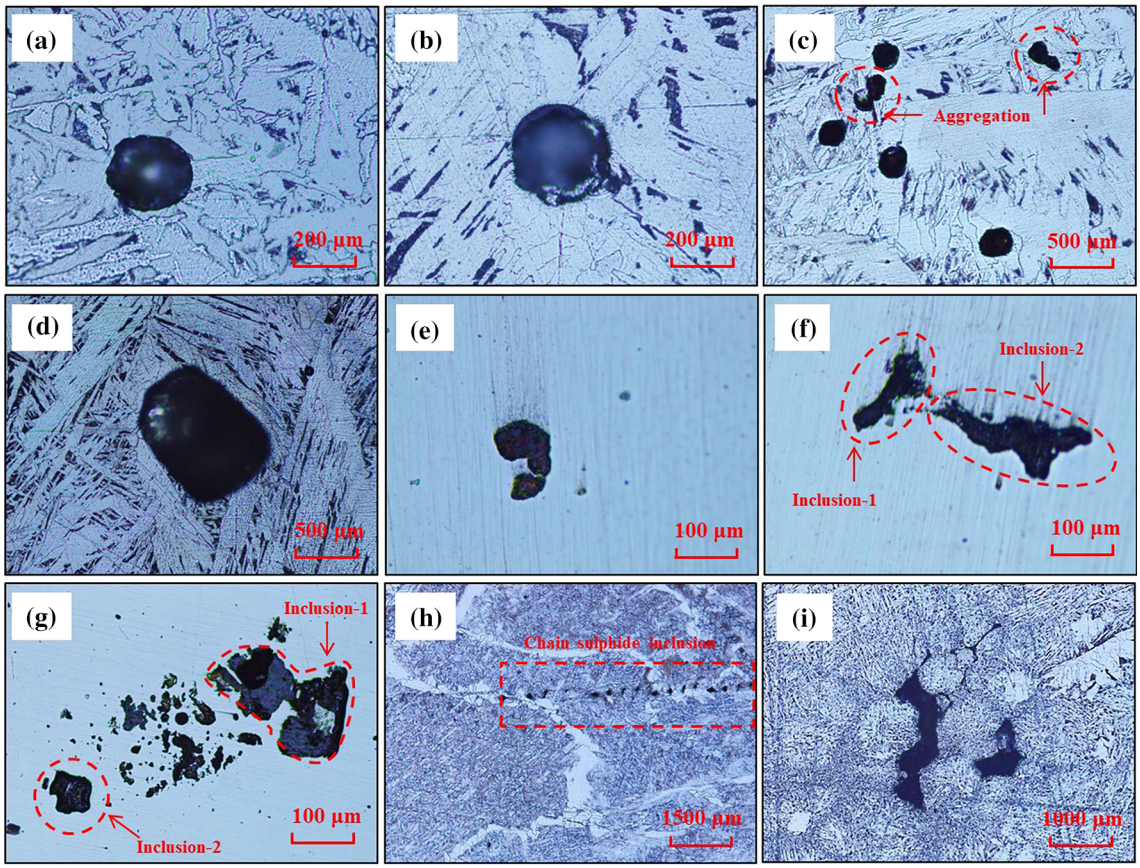

Fig. 4—Typical morphologies of MNMIs: (*a*) bubble with a shiny surface, (*b*) bubble with NMIs attachment, (*c*) separate inclusions group, (*d*) rectangular MNMI, (*e*) irregularly shaped MNMI, (*f*) irregularly shaped MNMIs treated as two single MNMIs, (*g*) NMI cluster, (*h*) chain sulfide MNMIs, and (*i*) shrinkage defects.

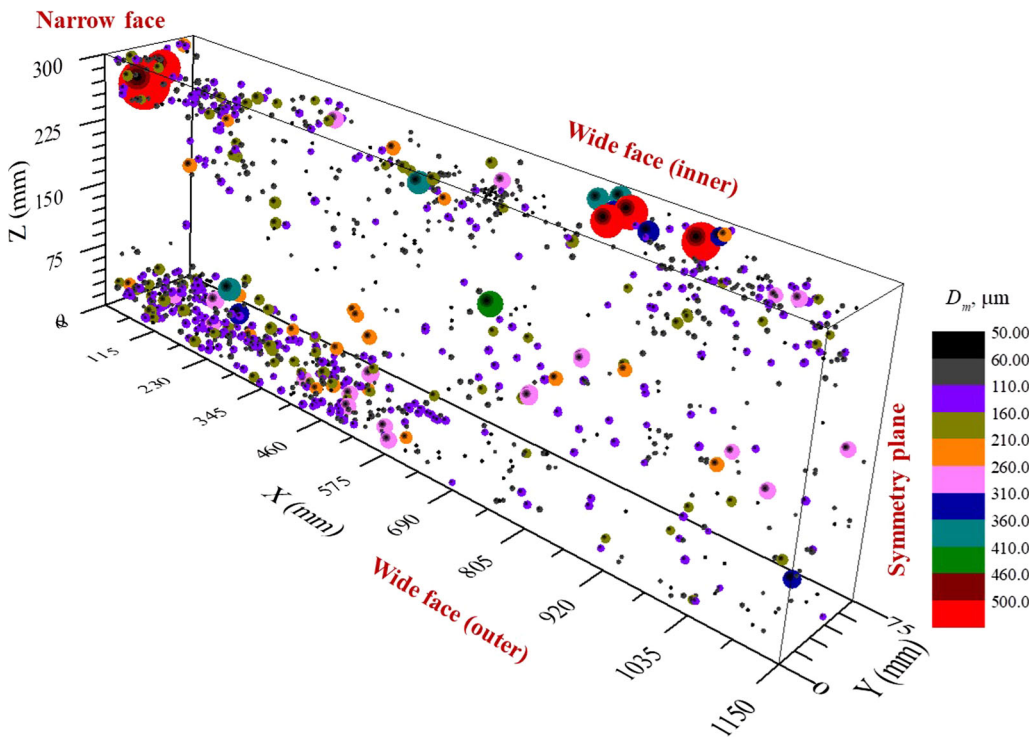

Fig. 5—Spatial distribution of MNMIs in the slab samples (for visualization, NMI sizes are enlarged 50 times).

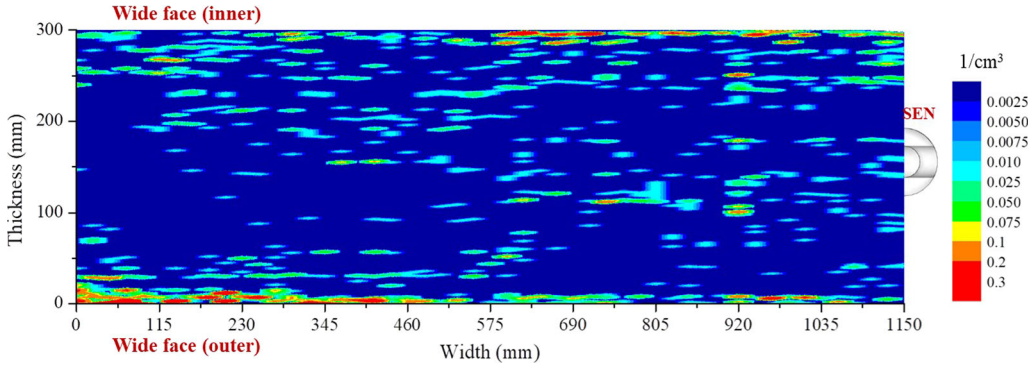

Fig. 6—Volume number density of MNMIs in the cross section of the slab samples.

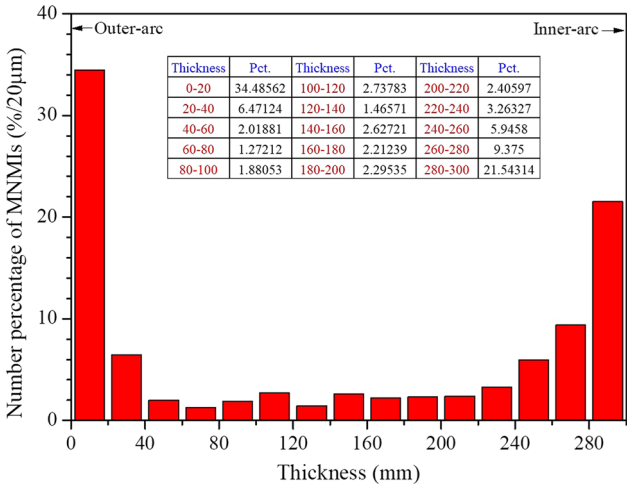

Thickness	Pct.	Thickness	Pct.	Thickness	Pct.
0-20	34.48562	100-120	2.73783	200-220	2.40597
20-40	6.47124	120-140	1.46571	220-240	3.26327
40-60	2.01881	140-160	2.62721	240-260	5.9458
60-80	1.27212	160-180	2.21239	260-280	9.375
80-100	1.88053	180-200	2.29535	280-300	21.54314

Fig. 7—Number percentage of MNMIs along the thickness direction of the slab.

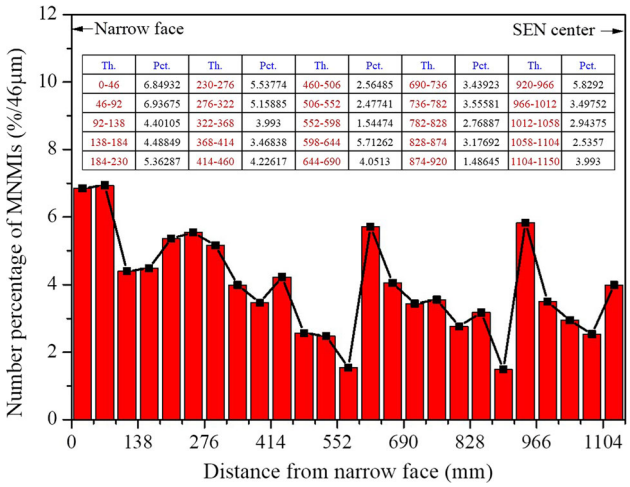

Th.	Pct.	Th.	Pct.	Th.	Pct.	Th.	Pct.	Th.	Pct.
0-46	6.84932	230-276	5.53774	460-506	2.56485	690-736	3.43923	920-966	5.8292
46-92	6.93675	276-322	5.15885	506-552	2.47741	736-782	3.55581	966-1012	3.49752
92-138	4.40105	322-368	3.993	552-598	1.54474	782-828	2.76887	1012-1058	2.94375
138-184	4.48849	368-414	3.46838	598-644	5.71262	828-874	3.17692	1058-1104	2.5357
184-230	5.36287	414-460	4.22617	644-690	4.0513	874-920	1.48645	1104-1150	3.993

Fig. 8—Number percentage of MNMIs along the width direction of the slab.

distribution of MNMIs in the cross section was not uniform. Most MNMIs were captured by the solidified shell close to the surfaces of wide faces, while fewer ones were found in the center. All the subsequent results were analyzed based on the current processed results of the same MNMI sampling resolution.

Figure 7 shows the number percentage of MNMIs along the thickness direction of the slab. More MNMIs were distributed beneath the wide faces. It can be clearly found that the number percentage of MNMIs was approximately 72 pct within 40 mm from the wide faces (Z = 0 to 40 mm and Z = 260 to 300 mm) and 28 pct in the center (Z = 40 to 260 mm) of the slab. Considering the MNMIs distribution within 20 mm from the wide faces, more MNMIs (34.49 pct) were captured at the outer arc of the caster than that at the inner arc (21.54 pct).

Figure 8 shows the number percentage of MNMIs along the width direction of the slab. Comparing with the MNMI distribution along the thickness direction (Figure 7), the MNMIs distribution along the width direction was more uniform. More MNMIs (13.8 pct within 92 mm from the narrow face) were captured by the solidified shell near the narrow face than those in the center (6.5 pct within 92 mm from the center). In addition, an interesting fluctuation behavior of MNMI number percentage distribution from the SEN to the narrow face can be found through the black line.

B. *Size Distribution*

The size distribution of MNMIs in the entire slab sample is shown in Figure 9. Fourteen MNMIs larger than 410 μm were not counted in this figure. In general, the number of MNMIs decreases with increasing the MNMI size. Most MNMIs were in the size range of 50 and 210 μm, which occupies more than 95 pct of the total number of MNMIs. The number of MNMIs larger than 290 μm was quite rare, which was approximately 1.6 pct (including the fourteen MNMIs larger than 410 μm). Based on the current MNMI size distribution, a probability number density function of MNMI diameter can be approximated based on the Farazdaghi–Harris equation, as follows:

$$\frac{n_k}{n_{\text{Total}}}\text{pct} = (0.048 + 1.425 \times 10^{-14} \cdot d_k^{5.78})^{-1}, \quad [4]$$

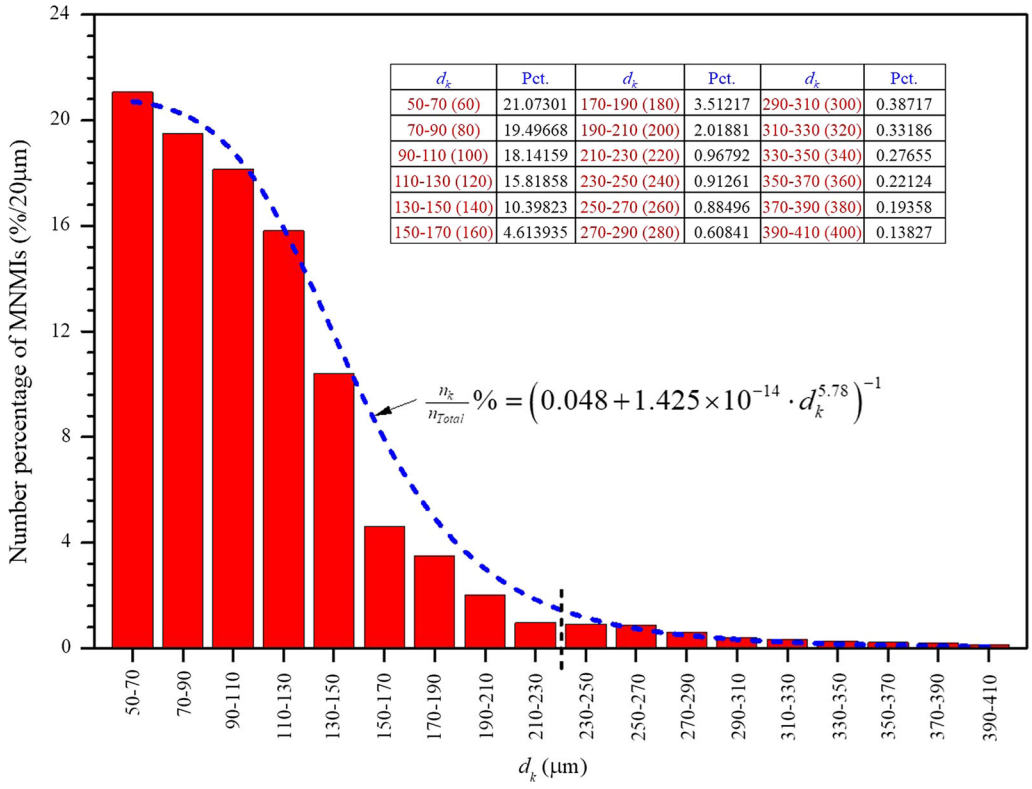

Fig. 9—Size distribution of MNMIs in all the slab samples.

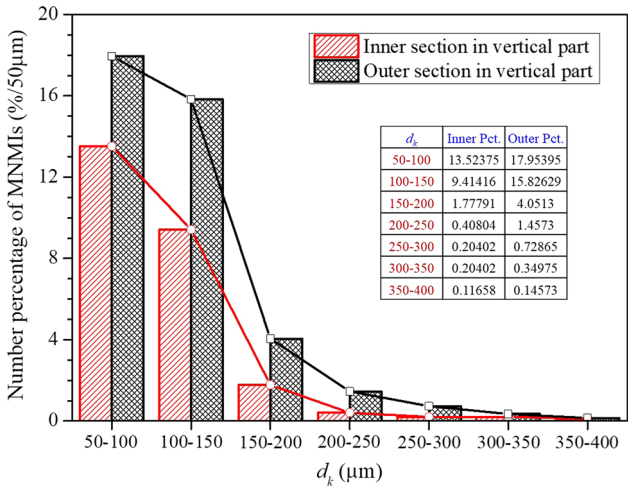

Fig. 10—Size distribution of MNMIs in vertical part of the caster.

where n_k is the number of MNMI-k. n_{Total} is total MNMI number in all the samples. d_k is the mean diameter of MNMI-k, the values ranging from 60 to 400 μm. The probability number density function can be used as the input source term of MNMIs at the inlet of SEN for the numerical simulations.

The growth of shell thickness is very important in the CC mold, because it controls the entrapment positions of NMIs. According to the previous numerical simulation,[27] the thickness of solid shell at the end (2.66 m below the top surface) of the vertical part of the caster yielded an average value of 30 mm. Therefore, this value of shell thickness was used as a criterion to distinguish the vertical part and the curved part of the slab. In another words, the initial 30-mm solid shell beneath the slab surface was formed in the vertical part. Figure 10 shows the size distribution of MNMIs in vertical part, from 0 to 30 mm thickness of the solidified shell, considering the difference between inner-curved section and outer-curved section of the slab. It is interesting to note that more MNMIs would be captured at the outer-curved section for various MNMI sizes.

Figure 11 shows the size distribution of MNMIs in bending part of the slab from 30 mm to the center. Compared with Figure 10, more MNMIs (over 66 pct) were captured in the vertical part; fewer MNMIs (less than 34 pct) were captured in the bending part. In contrary with the MNMI distribution in vertical part,

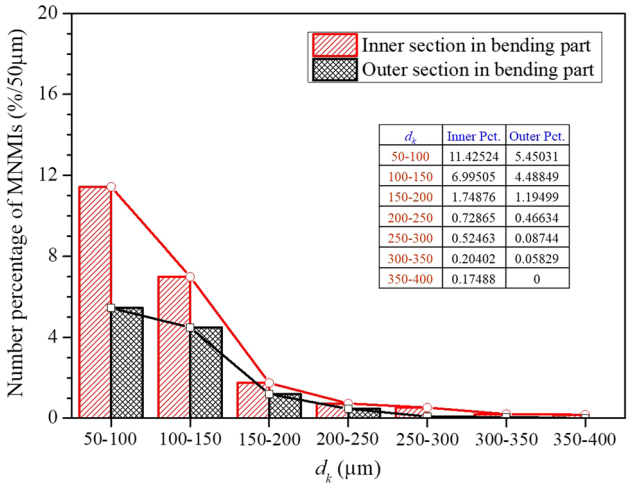

d_k	Inner Pct.	Outer Pct.
50-100	11.42524	5.45031
100-150	6.99505	4.48849
150-200	1.74876	1.19499
200-250	0.72865	0.46634
250-300	0.52463	0.08744
300-350	0.20402	0.05829
350-400	0.17488	0

Fig. 11—Size distribution of MNMIs in bending part of the caster.

more MNMIs were captured at the inner-curved section in the bending part, which occupies approximately 21.8 pct of the total MNMIs. Only 11.7 pct were captured at the outer-curved section.

V. SUMMARY DISCUSSIONS

This work provides an experimental benchmark of three-dimensional spatial distribution of MNMIs with diameter larger than 50 μm in a heavy CC slab. It is important to note that this experiment can be performed only once. It is difficult to repeat this experiment because it costs more than 4500 man-hour for the sample detection on the FDP. The 139 slices for each sample along the slab thickness represent good statistic of the MNMI distribution in the slab.

This call for contribution aims at proposing a set of experimental benchmark for verification and validation of mathematical models and numerical codes concerned with transport of MNMIs and finally distribution of MNMIs in the CC slab. Therefore, the present work does not provide any explanation for the results. The conclusions obtained are summarized as follows:

1. The morphology of the MNMIs was metallographically analyzed. Some typical morphologies of independent nearly spherical MNMIs, "bubble + NMIs," irregular-shaped MNMIs, and cluster MNMIs were found.
2. The number of the MNMIs of difference size classes was counted. More than 95 pct of MNMIs were in the size range of 50 and 210 μm. Only 1.6 pct of MNMIs were larger than 290 μm.
3. The 3D spatial distribution of MNMIs in the casting sample was reconstructed. The volume number density of MNMIs in the cross section of the sample was given.
4. A probability number density function of MNMI diameter was given, which can be used as the input source term of MNMIs at the inlet of SEN for the numerical simulations.
5. Further information about the size distribution of MNMIs along the thickness direction in both vertical section and bending section of the slab was reported.

ACKNOWLEDGMENTS

The authors are grateful for the support from National Natural Science Foundation of China (Nos. 51604070 and 51574068), Fundamental Research Funds for the Central Universities of China (No. N162504009), and China Scholarship Council (No. 201706085027).

REFERENCES

1. L. Zhang and B.G. Thomas: *ISIJ Int.*, 2003, vol. 43, pp. 271–91.
2. H. Jacobi: *Steel Res. Int.*, 2006, vol. 77, pp. 558–64.
3. K.D. Xu: *Acta Metall. Sin.*, 2009, vol. 45, pp. 257–69.
4. X. Zou, D. Zhao, J. Sun, C. Wang, and H. Matsuura: *Metall. Mater. Trans. B*, 2018, vol. 49, pp. 481–89.
5. C. Pfeiler, M. Wu, and A. Ludwig: *Mater. Sci. Eng. A*, 2005, vols. 413–414, pp. 115–20.
6. C. Pfeiler, B.G. Thomas, M. Wu, A. Ludwig, and A. Kharicha: *Steel Res. Int.*, 2008, vol. 79, pp. 599–607.
7. B.G. Thomas, Q. Yuan, S. Mahmood, R. Liu, and R. Chaudhary: *Metall. Mater. Trans. B*, 2014, vol. 45, pp. 22–35.
8. Z. Liu, B. Li, and M. Jiang: *Metall. Mater. Trans. B*, 2014, vol. 45, pp. 675–97.
9. S. Lee, S. Kim, and H. Lee: *J. Iron Steel Res. Int.*, 2011, vol. 18 (sup-2), pp. 220–26.
10. Z. Liu and B. Li: *Powder Technol.*, 2018, vol. 323, pp. 403–15.
11. Z. Liu and B. Li: *Powder Technol.*, 2016, vol. 287, pp. 315–29.
12. Z. Liu, B. Li, L. Zhang, and G. Xu: *ISIJ Int.*, 2014, vol. 54, pp. 2324–33.
13. H. Barati, M. Wu, A. Kharicha, and A. Ludwig: *Powder Technol.*, 2018, vol. 329, pp. 181–98.
14. S. Luo, B. Wang, Z. Wang, D. Jiang, W. Wang, and M. Zhu: *ISIJ Int.*, 2017, vol. 57, pp. 2000–09.
15. X. Deng, L. Li, X. Wang, Y. Ji, and G. Zhu: *Int. J. Miner. Metall. Mater.*, 2014, vol. 21, pp. 531–43.
16. H. Liao, S. Yang, J. Li, and J. Feng: *Metall. Mater. Trans. B*, 2017, vol. 48, pp. 3101–07.
17. J.C. Pandey, P.N. Choubey, and M. Raj: *Metall. Mater. Trans. A*, 2008, vol. 39A, pp. 1727–37.
18. R. Dekkers, B. Balanpain, P. Wollants, F. Haers, B. Gommers, and C. Vercruyssen: *Steel Res. Int.*, 2003, vol. 74, pp. 351–55.
19. Y. Ren, Y. Wang, S. Li, L. Zhang, X. Zuo, S. Lekakh, and K. Peaslee: *Metall. Mater. Trans. B*, 2014, vol. 45, pp. 1291–1303.
20. X. Zhang, Y. Ren, and L. Zhang: *Metall. Mater. Trans. A*, 2018, vol. 49, pp. 5469–77.
21. N. Kasai, H. Ookubo, and T. Nishi: *Tetsu-to-Hagané*, 2005, vol. 91, pp. 537–45.
22. L. Zhang, J. Zhi, F. Mei, L. Zhu, X. Jiang, J. Shen, J. Cui, K. Cai, and B.G. Thomas: *Ironmak. Steelmak.*, 2006, vol. 22, pp. 129–39.
23. Z. Deng, M. Zhu, B. Zhong, and S. Du: *ISIJ Int.*, 2014, vol. 54, pp. 2813–20.
24. S. Basu, S.K. Choudhary, and N.U. Girase: *ISIJ Int.*, 2004, vol. 44, pp. 1653–60.
25. H. Yin, H. Shibata, T. Emi, and M. Suzuk: *ISIJ Int.*, 1997, vol. 37, pp. 936–45.
26. Q. Wang, X. Zou, H. Matsuura, and C. Wang: *Metall. Mater. Trans. B*, 2018, vol. 49, pp. 18–22.

27. X. Zou, J. Sun, H. Matsuura, and C. Wang: *Metall. Mater. Trans. B*, 2018, vol. 49, pp. 2168–73.
28. Y. Miki, H. Ohno, Y. Kishimoto, and S. Tanaka: *Tetsu-to-Hagané*, 2011, vol. 97, pp. 423–32.
29. H. Esaka, Y. Kuroda, K. Shinozuka, and M. Tamura: *ISIJ Int.*, 2004, vol. 44, pp. 682–90.
30. X. Jin, Z. Lei, Z. Yu, H. Zhang, K. Deng, and Z. Ren: *Acta Metall. Sin.*, 2011, vol. 47, pp. 763–68.
31. L. Zhang, Y. Wang, E. Maetinez, and K.D. Peaslee: *Proceedings of TMS Conference*, 2012, pp. 3–16.
32. X. Li, B. Li, Z. Liu, R. Niu, and Q. Liu: *ISIJ Int.*, 2018, vol. 58, pp. 283–362.